Effect of the flow directions on a 100 cm² MCFC single cell with internal flow channels

CrossMark

Chang-Whan Lee, Mihui Lee, Min-Jae Lee, Seong-Cheol Chang, Sung-Pil Yoon, Hyung Chul Ham[*]*, Jonghee Han*[**]

Fuel Cell Research Center, Korea Institute of Science and Technology (KIST), 39-1 Hawolgok-dong, Sungbuk-gu, Seoul 136-791, Republic of Korea

A B S T R A C T

In this work, the effect of the flow direction on a newly designed 100 cm² cell frames with internal flow channels for molten carbonate fuel cells (MCFCs) was investigated using three-dimensional fluid dynamic analysis. Simulation results were compared with the experimental results for verification. From the simulation, the performance, pressure drop, flow field, and gas mole fractions inside the cell frame were studied. In the performance of the single cell, only small difference was observed between co-flow and counter-flow; however, counter-flow resulted in a more uniform distribution of the current density without any hot-spots. For counter-flow, a uniform distribution of the current density could be achieved by controlling the current density or gas utilization.

© 2016 Published by Elsevier Ltd on behalf of Hydrogen Energy Publications LLC.

Introduction

Molten carbonate fuel cells (MCFCs) are being developed for clean and efficient power conversion. MCFCs are a promising source of renewable energy for the high-efficiency cogeneration of electricity and heat with minimal environmental impact [1]. MCFCs operate at a high temperature of approximately 650 °C. Because of the high temperature, precious metal catalysts are not required during the operation. A schematic figure of MCFCs is presented in Fig. 1.

Most experimental studies on high temperature fuel cells are expensive and time-consuming. By modeling MCFCs numerically, quantitative results inside MCFCs such as the distribution of temperature, current density, mole fraction of each gas, pressure distribution and velocity distribution can

be obtained. In addition, the performance of MCFCs can be calculated over wide ranges of temperature, gas utilizations, and gas compositions. From the simulation results, it is possible to determine the appropriate operating conditions for high-performance and long-term operation.

Many approaches to the calculation of voltage losses for MCFCs have been developed. Wolf and Wilemski [2] developed a two-dimensional numerical model to predict the non-isothermal performance of MCFCs. Yuh and Selman [3] investigated the polarizations of MCFCs with various gas compositions and temperatures. The anode and cathode polarizations were derived from single cell experiments using partial pressure of reactive gases and temperature when the concentration losses are not dominant. Bosio et al. [4] developed a performance model based on a combined experimental

Nomenclature

c_j	molar concentration of species j
C_p	specific heat capacity, $J\,kg^{-1}\,K^{-1}$
$D_{i,j}$	binary diffusion coefficient, $m^2\,s^{-1}$
D_j	diffusion coefficient of species j, $m^2\,s^{-1}$
E_0	standard potential, V
E_{eq}	equilibrium cell potential, V
F	Faraday's constant (96,485 $C\,mol^{-1}$)
g	gravitational constant (9.8 $m\,s^{-2}$)
h	heat transfer coefficient, $W\,m^{-2}\,K^{-1}$
i	local current density, $mA\,cm^{-2}$
i_{avg}	average current density, $mA\,cm^{-2}$
k_j	thermal conductivity of species j, $W\,m^{-1}\,K^{-1}$
K_{wgs}	equilibrium constants of water-gas shift reaction
m_j	mass fraction of species j
M_j	molecular weight of species j, $g\,mol^{-1}$
p_j	partial pressure of species j, $N\,m^{-2}$
P	total pressure, $N\,m^{-2}$
Pr	Prandtl number
r	reaction rate ($mol\,s^{-1}$)
R	universal gas constant (8.3145 $J\,mol^{-1}\,K^{-1}$)
R_a	anode polarization resistance, $\Omega\,m^2$
R_c	cathode polarization resistance, $\Omega\,m^2$
Re	Reynold's number
R_{irr}	total polarization resistance, $\Omega\,m^2$
R_{ohm}	ohmic resistance, $\Omega\,m^2$
S_j	source term of j_{th} equation
T	temperature, K
u_j	velocity of species j, $m\,s^{-1}$
V_{cell}	Cell voltage, V
X_j	Mole fraction of species j
ΔH	Enthalpy change, $J\,mol^{-1}$

Greek symbols

β	coefficient of volumetric expansion, K^{-1}
δ	characteristic length, m
μ_i	dynamic viscosity of species i, $kg\,m^{-1}\,s^{-1}$
ν_i	kinematic viscosity of species i, $kg\,m^{-1}\,s^{-1}$
ρ	density of the gas, $kg\,m^{-3}$
σ_{ij}	Lennard–Jones parameter
Ω_D	collision integral

Subscript

a	anode
c	cathode
cond	conduction between electrodes and cell frames
cf	cell frame
E	overall cell reaction
elec	electrodes
f	forced convection
g	gas
n	natural convection
wgs	water gas shift reaction

Fig. 1 – Schematic figure of MCFCs.

describing ohmic resistance, anode resistance and cathode resistance are determined experimentally.

In addition to performance models, gas flow and thermal characteristics of MCFCs affect the accuracy of the simulation model. He and Chen [6] developed an simulation model for MCFC stacks by taking account of the heat transfer and gas transport under transient conditions. Koh et al. [7] investigated numerical simulation parameters such as grid setting, thermal and gas properties, and thermal radiation. Hirata et al. [8] evaluated effects of the gas channel height on the distribution of the reactive gas concentration using computational fluid dynamics (CFD) analysis. Kim et al. [9] studied the effects of water-gas shift reaction on MCFCs. Ma et al. [10] investigated the effects of the non-uniform inlet flow rate from channel to channel on the fuel cell performance. For the precise simulation, it is necessary to use proper flow characteristics model with electrochemical reaction of MCFCs. In the simulation of MCFC stacks, the gas flow channels were assumed to be porous media in order to increase computational efficiency [11,12]. The flow channels made by the current collectors were considered with the porous media with equivalent properties of the porous media. In the simulation model with porous media, the detailed characteristics of the flow channel [10] were not considered. In addition, the heat transfer between the current collector and gases was not properly considered in the simulation model.

In this work, a newly designed 100 cm^2 single cell with internal flow channels for MCFCs was three-dimensionally modeled for precise prediction. The gas flow channel in the cell frame was modeled three-dimensionally instead of using porous media [11,12]. The effects of the flow channel and relative flow direction such as co-flow and counter-flow were investigated. In order to verify the proposed simulation model, simulation results were compared with experimental results. The distributions of the gas mole fraction, current density, flow field, temperature, and polarizations were investigated using the simulation results. From the simulation results, the operating conditions required to achieve uniformly distributed current densities were studied.

Experimental conditions and cell frames with internal flow channels

In the experiments for the MCFC single cell, a Ni – 5 wt% Al anode with the thickness of 0.7 mm, a lithiated NiO cathode with the thickness of 0.7 mm, and γ-LiAlO$_2$ matrices with the

and theoretical approach mostly derived from previous models developed for solid oxide fuel cells. Morita et al. [5] employed Arrhenius-type equations to describe voltage losses in MCFCs. Parameters in Arrhenius-type equations for
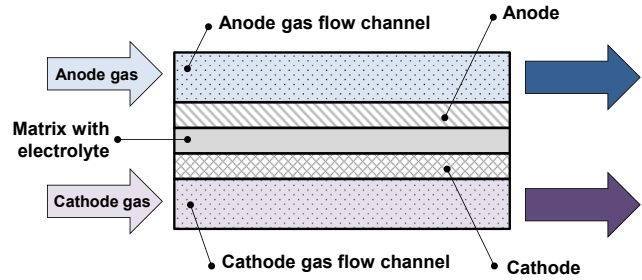
thickness of 1.2 mm were used. The size of the cell frame was 130 mm (length) × 130 mm (width) × 30 mm (height). The active area of the cell was 10,000 mm². The height and width of each flow channel is 3 mm. For the cell frame, AISI 316L was used. The electrolyte green sheet Li_2CO_3 and K_2CO_3 (62:38) were used. AISI 316L was used for the anode cell frame, the cathode cell frame and the cathode current collector [13]. For the anode current collector, a perforated nickel plate was used.

In this work, cell frames with internal flow channels were utilized. A schematic figure of the anode cell frame is presented in Fig. 2(a). The input gas was separated into the two gas lines. The gas lines were inserted in the cell frame. Gas lines were separated into three lines in the cell frame. Three lines are connected to the gas distribution space. After passing the gas distribution space, gases are distributed to the gas channels in the cell frame. Gases flow through the channel and electrodes, and an electrochemical reaction occurred. A cross section of the section A is presented in Fig. 2(b).

The cell frame with internal flow channels has advantages in controlling the temperature of the cell frame and components. In addition, the gas uniformity of the gas flow channel increases by separating the gas flow line in the cell frame. The gas flow line outside the cell frame acts as a pre-heater.

In order to investigate the effect of the relative gas flow direction, single cells of MCFCs with co-flow and counter-flow were employed in this work. The flow direction of the anode gas and the cathode gas was the same in the co-flow type single cell. The flow direction of the cathode gas was the reverse direction of the flow direction of the anode gas in the counter-flow type cell.

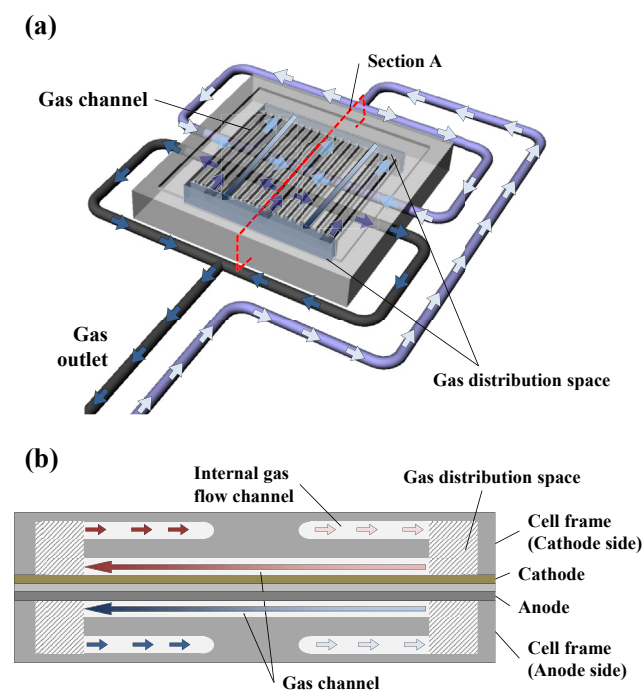Fig. 3(a) shows the anode cell frame and components of the MCFC single cell. The counter-flow cell frame was prepared by changing the gas input lines of the cell frame of the co-flow type. As illustrated in Fig. 3(b), the inlet line of the cathode flow was modified. The cathode gas line was bent twice to heat the cathode flow gas before inserting the cell frame. Using the cathode cell frame shown in Fig. 3(b) and the normal anode cell frame, the MCFC single cell with counter-flow could be operated without any problems.

After assembling the cell frames and components, the single cell was inserted in the heat chamber using a hydraulic press. To ensure close contact among the components of MCFC, a sealing pressure of 0.2 MPa was applied to the cell using the hydraulic pressure, as illustrated in Fig. 3(c).

The operating conditions and gas compositions are summarized in Table 1. The single cell was operated at 620 °C. The gas utilization for the anode side (H_2) and the cathode side (O_2 and CO_2) were fixed to 0.4 at 150 mA/cm².

Simulation model

Reaction model of MCFCs

Anode gas and cathode gas flow through the gas flow channel. The pressure and velocity of the gas were calculated using the momentum conservation equation presented in Eq. (1). The continuity equation is presented in Eq. (2). The chemical transport was calculated using Eq. (3). The energy balance equation is presented in Eq. (4)

$$\frac{\partial}{\partial x_j}(\rho u_j u_i) = -\frac{\partial P}{\partial x_i} + \frac{\partial}{\partial x_i}\left(\mu \frac{\partial u_i}{\partial x_j}\right) + S_i \tag{1}$$
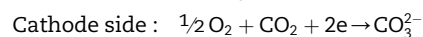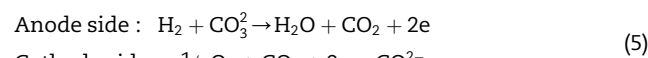
$$\frac{\partial}{\partial x_j}(\rho u_j) = S_j \tag{2}$$

$$\frac{\partial}{\partial x_j}(\rho u_j m_k) = \frac{\partial}{\partial x_j}\left(\rho D_{j,k}\frac{\partial m_k}{\partial x_j}\right) + S_k \tag{3}$$

$$u_j\frac{\partial}{\partial x_j}(\rho C_P T_g) = \frac{\partial}{\partial x_j}\left(k_j\frac{\partial T_g}{\partial x_j}\right) - \sum_k h_k(T_g - T_k) + \sum Q \tag{4}$$

where u_j is the velocity of the species j, m_k is the mass fraction of species k, S_j is the net mass production of species j, $D_{j,k}$ is the multi-component diffusivity, and Q is the heat generation.

The reactions of MCFCs on the anode side and the cathode side are

$$\text{Anode side}: \quad H_2 + CO_3^2 \rightarrow H_2O + CO_2 + 2e$$
$$\text{Cathode side}: \quad \frac{1}{2}O_2 + CO_2 + 2e \rightarrow CO_3^{2-} \tag{5}$$

The porous matrix is assumed to be filled with electrolyte composed of Li_2CO_3 and K_2CO_3. In this work, the reaction of MCFCs is assumed to occur on the surface of the matrix. The surface of the matrix is called the reaction surface [12].

In MCFCs, equilibrium cell potential (E_{eq}) was calculated from the gas partial pressures and standard potential. From the change in the molar Gibbs free energy (ΔG), the standard potential (E_0) is expressed as Eq. (6). E_{eq} of MCFCs is expressed as Eq. (7). The reaction rate (r) in the reaction layer is expressed as Eq. (8).

(a)

(b)

Fig. 2 – Structure of the cell frame with internal flow channels: (a) schematic figure of the cell frame and (b) sectional view (section A).
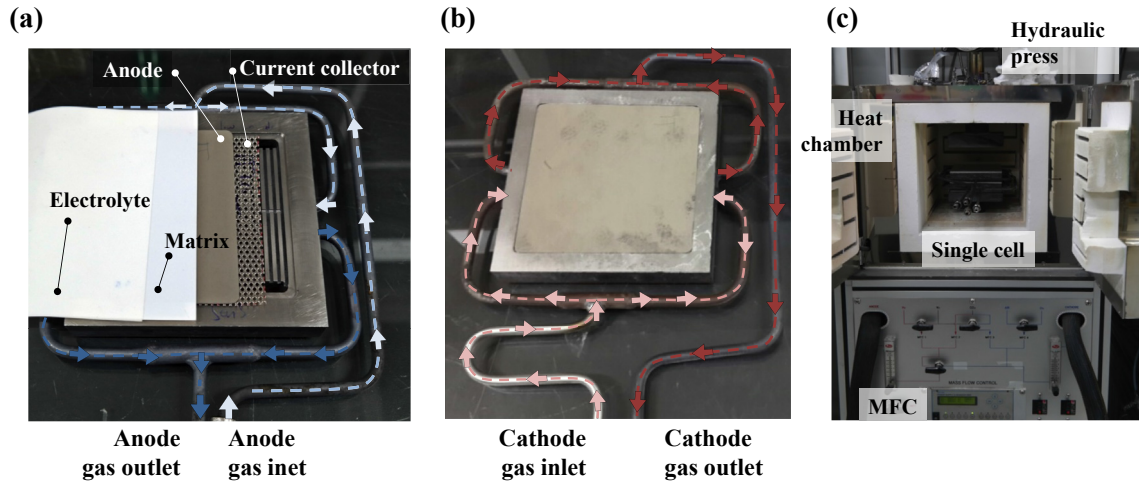
Fig. 3 – Experimental set-up for the MCFC single cell: (a) anode cell frame and components of the MCFC single cell (b) Cathode side cell frames for counter-flow, and (c) MCFC test equipment.

$$E_0^{x,y} = -\frac{\Delta G}{2F} = -\frac{-243730 + 48.996 \times T^{x,y} + 2.474 \times 10^{-3} \times (T^{x,y})^2}{2F} \tag{6}$$

$$E_{eq}^{x,y} = E^{0,xy} + \frac{RT}{2F} \ln\left(\frac{P_{H_2,a}^{x,y} P_{CO_2,c}^{x,y} \sqrt{P_{O_2,c}^{x,y}}}{P_{H_2O,a}^{x,y} P_{CO_2,a}^{x,y}}\right) \tag{7}$$

$$r^{x,y} = \frac{i^{x,y}}{2F} \tag{8}$$

In the simulation, the voltage of the cell was assumed to be uniform with the value of V_{cell} at the reaction surface [14]. In this work, the anode and cathode polarization model suggested by Yuh and Selman [3] was adopted. They divided polarization resistance of MCFCs into the anode polarization resistance, the cathode polarization resistance, and the ohmic resistance. Each polarization resistance was correlated using linear multiple regression in various gas conditions. The local current density ($i^{x,y}$) was calculated using Eq. (11).

$$R_a^{x,y} = 2.27$$
$$\times 10^{-9} \exp\left(\frac{6435}{T^{x,y}}\right)\left(P_{H_2}^{x,y}\right)^{-0.42}\left(P_{CO_2}^{x,y}\right)^{-0.17}\left(P_{H_2O}^{x,y}\right)^{-1.0} \left[\Omega \, m^2\right] \tag{9}$$

$$R_c^{x,y} = 7.505 \times 10^{-10} \exp\left(\frac{9298}{T^{x,y}}\right)\left(P_{O_2}^{x,y}\right)^{-0.43}\left(P_{CO_2}^{x,y}\right)^{-0.09} \left[\Omega \, m^2\right] \tag{10}$$

$$i^{x,y} = \frac{E_{eq}^{x,y} - V_{cell}}{R_{irr}^{x,y}} = \frac{E_{eq}^{x,y} - V_{cell}}{R_a^{x,y} + R_c^{x,y} + R_{ohm}^{x,y}} \tag{11}$$

The ohmic loss was modeled with an Arrhenius type equation [15]. The variables in Eq. (12) were determined from experimental results. The ohmic loss with respect to the operating temperature was measured using electrochemical impedance spectroscopy (EIS) analysis [16]. The ohmic loss is expressed as follows

$$R_{ohm}^{x,y} = 0.32 \times 10^{-4} \exp\left[4026\left(\frac{1}{T^{x,y}} - \frac{1}{923}\right)\right] \left[\Omega \, m^2\right] \tag{12}$$

The source term on the reaction surface is expressed as follows

$$\text{Anode side}: D_{m,k}\frac{\partial c}{\partial z} = \frac{i}{2F}$$
$$\text{Cathode side}: D_{m,k}\frac{\partial c}{\partial z} = \frac{i}{4F} \tag{13}$$

The heat generated from the electrochemical reaction was determined from the sum of the enthalpy change of the reaction minus the electrical power reduced. The heat from the electrochemical reaction is presented in Eq. (14) [17].

$$Q_E = i\left(-\frac{\Delta H_E}{2F} - V_{cell}\right) \tag{14}$$
$$\Delta H_E = -(240506 + 7.3835T) \, [J/mol]$$

The water-gas shift (WGS) reaction expressed in Eq. (15) was modeled in the simulation model [9]. The concentration of carbon monoxide (CO) was based on the equilibrium constant expressed in Eq. (16).

Table 1 – MCFC single-cell operating conditions and components.		
Temperature		620 °C
Pressure		1 atm
Sealing pressure		0.2 MPa
Gas utilization (Anode H_2/cathode O_2 and CO_2)		0.4 at 150 mA/cm^2
Gas flow rate	Anode	357 sccm
	Cathode	952 sccm
Input gas composition	Anode	H_2:CO_2:H_2O = 0.72:0.18:0.1
	Cathode	Air:CO_2 = 0.7:0.3

Anode side : $H_2O + CO \leftrightarrow CO_2 + H_2$ (15)
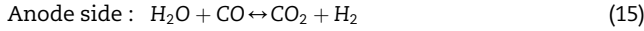
$$K_{WGS} = \frac{[P_{H_2}][P_{CO_2}]}{[P_{CO}][P_{H_2O}]}$$
$$= 157.02 - 0.4447T + 4.2777 \times 10^{-4}T^2 - 1.3871 \times 10^{-7}T^3$$
(16)

The equilibrium constant of the WGS reaction can be expressed using temperature (T) as demonstrated in Eq. (16). The reaction rate of the WGS reaction is so fast that the concentration of CO was directly calculated from Eq. (16) [18]. The enthalpy change in the WGS reaction is expressed by Eq. (17) [19].

$$\Delta H_{WGS} = -43729 + 9.4657T \text{ [J/mol]}$$
(17)

Heat transfer model

Three fundamental modes of heat transfer are conduction, convection and radiation. The effect of thermal radiation is negligible, and was not considered in the simulation model [7]. The current collector was modeled as a film with the conductivity of 25 W m^{-1} K^{-1} and a thickness of 0.7 mm. Heat conduction between the metallic cell frame and the electrode was calculated using the thermal resistance. Three types of heat transfer occurred in the cell frame: natural convection between the heat chamber and the cell frame, forced convection between the gas and the gas flow channel and conduction between the cell frame and the MCFC components as illustrated in Fig. 4.

Heat transfer due to conduction occurs between the metallic cell frame and the electrode. There is thermal resistance between the cell frame and the electrode because of the sealing pressure. The heat transfer between the metallic cell frame and the electrode (Q_c) is expressed as Eq. (18). In this
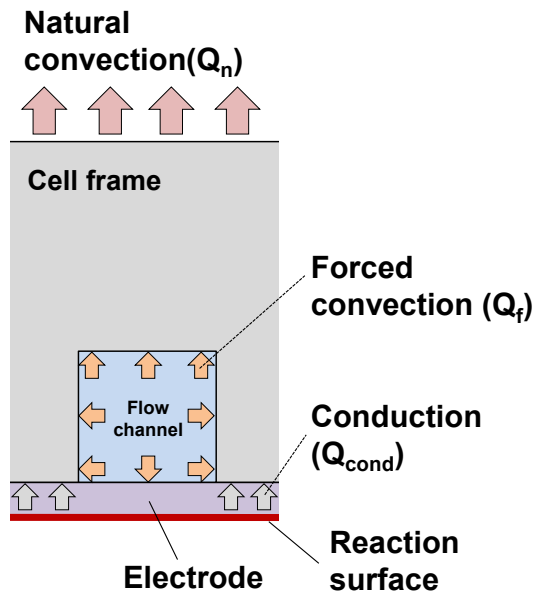

Fig. 4 – Heat transfer model of the cell frame.

work, a coefficient (h_c) of 593.1 W m^{-2} K^{-1} from the previous study [20] was adopted.

$$Q_{cond} = h_{cond}A(T_{elec} - T_{cf})$$
(18)

At the outer edges of the cell frame, natural convection due to the heat chamber occurred. The heat from the heat chamber (Q_n) is expressed as follow:

$$Q_n = h_nA(T_{cf} - T_\infty), \quad h_n = Nu_{air}\frac{k_{air}}{D_h}$$
$$Nu_{air} = 0.54 \cdot \left(\frac{1}{T}\frac{g\beta(T_{cf} - T_\infty)\delta}{v_{air}}Pr_{air}\right)^{0.25}$$
(19)

where h_n is the natural convection coefficient in the heat chamber, T_∞ is the temperature of the heat chamber, T_C is the temperature of the cell frame, Nu_{air} is the Nusselt number of the ambient air, k_{air} is the conductivity of the air, D_h is a geometric constant, Pr_{air} is the Prandtl number of air, g is the gravitational acceleration, β is the coefficient of volumetric expansion of air, δ is the characteristic length, and v_{air} is the dynamic viscosity of air.

Inside the flow channel, heat transfer between the cell frame and gas occurs. At that surface, forced convection due to the gas flow occurs. The heat due to the forced convection is

$$Q_f = h_fA(T_g - T_{cf}), \quad h_f = Nu_g\frac{k_g}{D_h}$$
(20)

where k_g is the heat conductivity of the mixed gas in the flow channel, and T_g is the temperature of the mixed gas. For a rectangular flow channel, D_h is the width of the flow channel. Nu_g of the constant heat rate and the rectangular flow channel is 3.61 [21]. The values of the natural and forced heat convection coefficient were updated for each calculation.

Material properties

The thermal properties of AISI 316L, the cathode, and the anode at 620 °C are summarized in Table 2.

For the precise simulation of MCFCs, the appropriate thermal properties of the mixture gases of the anode and cathode gas are required. The composition and properties of mixture gases varies with respect to the temperature, gas compositions, and electro-chemical reactions. The density (ρ), specific heat (C_p), thermal conductivity (k), and viscosity of the mixture gases (μ) are calculated considering the composition of mixture gases and the temperature [7]. The density and the specific heat of the anode and cathode gas were calculated using the ideal gas law. The viscosity and conductivity of the gas were calculated using the gas mixture rule. The multi-component diffusivity ($D_{i,j}$) was calculated using Eq. (21).

Table 2 – Thermal properties of AISI 316L, the anode, and the cathode [22].			
	AISI 316L	Anode (Ni-Al)	Cathode (NiO)
Density (kg m^{-3})	7800	8220	6794
Heat capacity (J kg^{-1} K^{-1})	500	444	44,352
Thermal conductivity (W m^{-1} K^{-1})	25	78	5.5

$$D_{i,j} = \frac{1 - X_i}{\sum\limits_{i \neq j} \frac{X_i}{D_{ij}}}, \quad D_{ij} = \frac{0.001858T^{\frac{3}{2}}\left[\frac{M_i + M_j}{M_i M_j}\right]^{\frac{1}{2}}}{P\sigma_{ij}^2 \Omega_D} \qquad (21)$$

where M_i is the molecular weight of species i, D_{ij} is the binary diffusion coefficient σ_{ij} is Lennard−Jones parameters and Ω_D is the collision integral [22].

Simulation model

It is assumed that the WGS reaction reaches equilibrium before the gases are inserted into the cell frame. The temperature of the input gas was assumed to be identical with the operating temperature. The input gas composition was calculated from the normal gas composition using the WGS reaction. The composition of the anode input gas at 620 °C is $H_2:CO_2:H_2O:CO = 0.617:0.077:0.203:0.103$.

For a simple calculation, symmetric boundary conditions are used. As shown in Fig. 5, a half model with symmetric boundary condition was used. The plane in the center of the simulation model was used as the symmetric plane. The simulation model was composed of two parts, the metallic
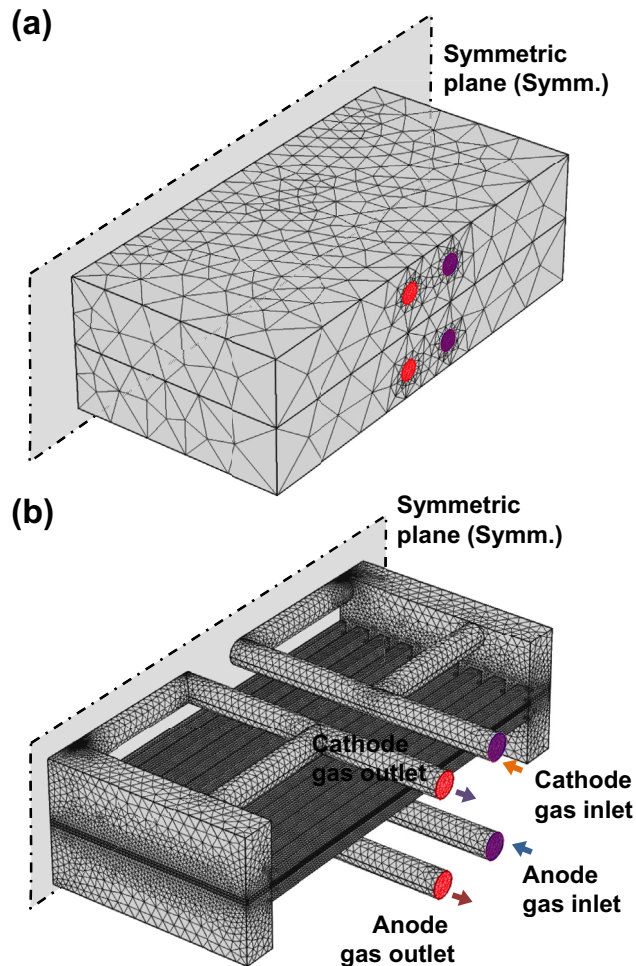

(a)

Symmetric plane (Symm.)

(b)

Symmetric plane (Symm.)

Cathode gas outlet

Cathode gas inlet

Anode gas inlet

Anode gas outlet

Fig. 5 − Simulation model for the three-dimensional analysis of the frame cell (532,714 tetrahedral elements): mesh of the (a) cell frame and (b) flow channel.

structure and the flow channel including the anode and the cathode. In the cell frame, which is the metallic structure, the variable is the temperature only. A coarse mesh was used for the cell frame, as shown in Fig. 5(a). The number of elements for the cell frame was 29,842.

For the precise simulation, the gas flow channel was meshed using very fine tetrahedral elements. The mesh of the gas flow channel inside the cell frame is shown in Fig. 5(b). The gas flow channel outside the cell frame was not modeled in the simulation. The components of MCFC such as the cathode and the anode were modeled as porous materials. The anode and cathode gas channels are modeled with very fine tetrahedral elements similar to the gas flow channel. For the mesh of the gas flow channel, 532,714 tetrahedral elements were used. The gas flow in the flow channels is in laminar form, because the low speed of gas flow (smaller than 2 m/s) results in low Reynolds number.

In the simulation, the commercial CFD code COMSOL multi-physics v14 [23] was employed in order to calculate the steady state such as the energy balance, species balance, momentum and continuity equations. In the simulation, the voltage of the cell (V_{cell}) was assumed to be uniform at the reaction surface [14]. For a given V_{cell}, the calculation begins with an initial current density distribution. In the simulation, the relative error of variables computed as the weighted Euclidean norm was considered as a convergence criterion. The solution was judged to be converged when the relative error was less than relative tolerance (10^{-6}). After convergence, distribution of local current density, temperature, velocity, and species concentration are calculated with respect to V_{cell}. The average current density (i_{avg}) was obtained by taking the average of current density over the reaction surface.

Results

Comparison of the simulation result with the experimental result

For the verification of the simulation model, the simulation results of the co-flow type single cell were compared with the experimental results with respect to the operating temperature (650 °C, 620 °C, 600 °C, and 580 °C), gas utilizations (0.4, 0.6, and 0.8), and gas compositions. The operating conditions with different gas compositions are listed in Table 3. Gas condition of Case A is the normal gas condition in Table 1.

Table 3 − Operating conditions with different gas compositions.

	Anode gas (357 sccm)			Cathode gas (952 sccm)	
	H_2	CO_2	H_2O	CO_2	Air
Case A	0.72	0.18	0.1	0.3	0.7
Case B	0.6	0.3	0.1		
Case C	0.45	0.45	0.1		
Case D	0.72	0.18	0.1	0.2	0.8
Case E				0.1	0.9

Fig. 6(a) presents the average current density (i_{avg}) – cell voltage (V_{cell}) characteristics of MCFCs single cell with respect to the operating temperatures. The gas utilization of the anode gas and the cathode gas was 0.4 and the gas condition was case A. As the operating temperature decreases, the performance of the cell also decreases. Fig. 6(b) presents the I-V characteristics with respect to the gas utilization. The operating temperature was 620 °C and the gas condition was case A. The decreased gas utilization means less gas were inserted to the cell. When u_f is 0.8, the total flow rate of each gas is half of the normal condition. As the gas utilization increases, the performance of the cell decreases.

Fig. 6(c) and (d) present the simulation results and the experimental results with other gas conditions. The total flow rate of the anode gas and cathode gas are fixed. The mole fraction of each gas conditions are listed in Table 3. The experiments and simulation was conducted at 620 °C. As the mole fraction of H_2 in the anode side decreases, the open circuit voltage and the performance of the cell decrease. As CO_2 in the cathode side decreases, the open circuit voltage and the performance of the cell decrease. In case E, CO_2 for electrochemical reaction was lack and the mass transfer resistance increased. Error between the simulation results and the experimental results increases as the mass transfer resistance increases.

In all cases, the performance of the cell can be predicted precisely when the concentration loss is not dominant. The difference between the simulation results and the experimental results increases as the average current density increases. The simulation model overpredicts the performance of the single cell at high current densities, because the polarizations of MCFCs were modeled in the gas conditions when the concentration losses are not dominant.

Effects of the gas flow directions in 100 cm^2 single cell

The IV characteristics of the co-flow type and counter-flow type single cells at 620 °C and normal gas condition (Case A in Table 3) are presented in Fig. 7. The experimental results were compared with the simulation results. The performance of the counter-flow type single cell was slightly better than that of the co-flow type single cell. In the experiments, the voltage of the co-flow type single cell was 0.818 V at 150 mA/cm^2 and the voltage of the cell with counter-flow type was 0.822 V at 150 mA/cm^2. In the simulation, the voltage of co-flow type single cell was 0.817 V at 150 mA/cm^2 and the voltage of the cell with counter-flow type was 0.823 V at 150 mA/cm^2. The performance difference at 150 mA/cm^2 between counter-flow and co-flow was 4 mV for the experimental results and 6 mV for the simulation result. The
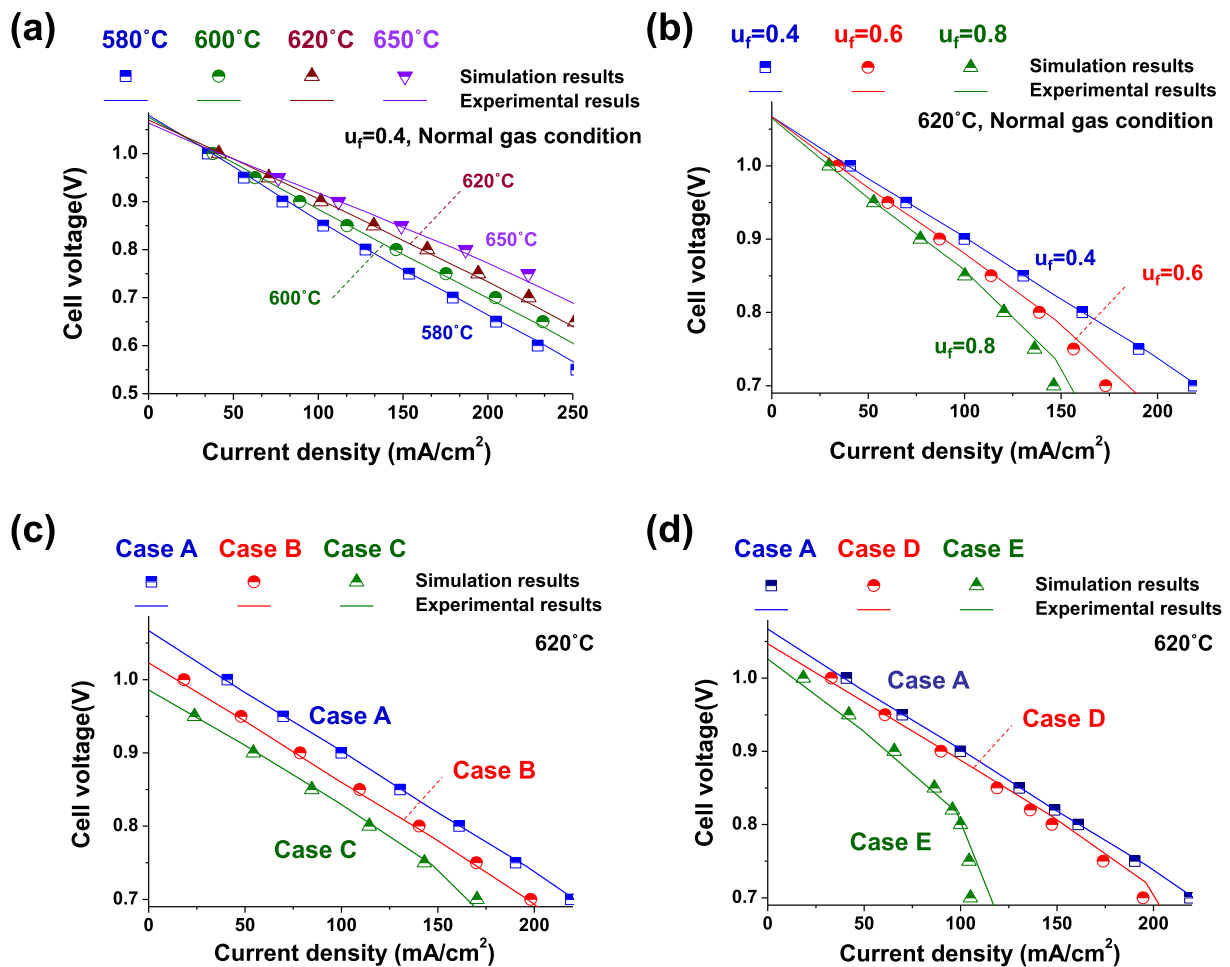

Fig. 6 – Performance of the single cell: (a) Effect of the operating temperature (b) Effect of the gas utilization (c) with different anode gas compositions, and (d) with different cathode gas compositions.
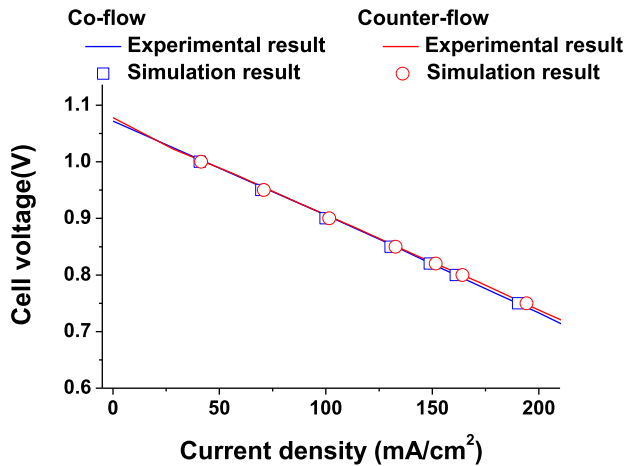
Fig. 7 – **Performance of the single cell with co-flow and counter-flow.**

performance difference between counter-flow and co-flow was very small compared with the cell voltage at 150 mA/cm^2.

However, the current density distribution differed more substantially. Fig. 8(a) plots the current density distribution of the co-flow type single cell at 150 mA/cm^2. The dotted line in the center represents the symmetric line. The high current occurred near the gas input line, and the current density decreased along the gas flow channel. The difference between the maximum and minimum value of the current density was 92.1 mA/cm^2.

Fig. 8(b) shows the current density distribution of the counter-flow type single cell at 150 mA/cm^2. The shape of the distribution was completely different from that of the co-flow type cell. The current density decreased along the flow
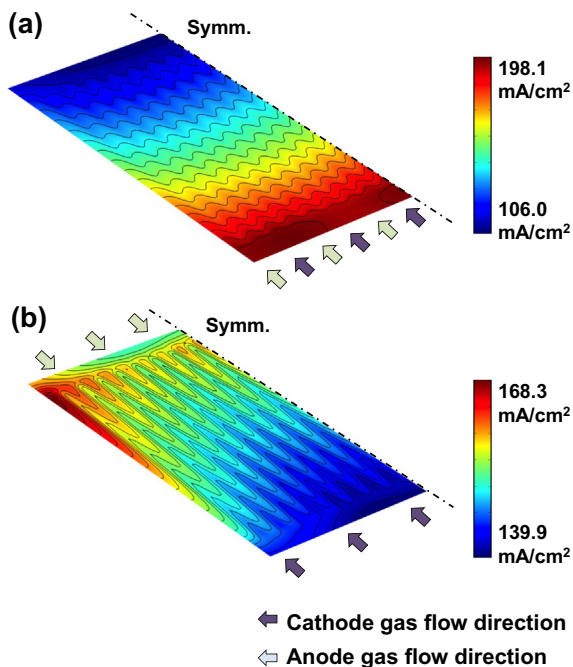

Cathode gas flow direction
Anode gas flow direction

Fig. 8 – **Current density distribution of the MCFC single cell at 150 mA/cm^2 and 620 °C: (a) co-flow and (b) counter-flow.**

direction of the anode gas. The difference between the maximum and minimum value of the current density was 28.4 mA/cm^2. The current density was more uniformly distributed for the counter-flow type single cell.

The temperature distributions of the reaction surface and cell frames are presented in Fig. 9. The temperature of the furnace was 620 °C. The temperature of the single cell increased because of the electrochemical reaction. At the average current density of 150 mA/cm^2, the maximum temperatures were 623.92 °C for the co-flow type cell and 624.11 °C for the counter-flow type cell. The temperature near the anode gas input was higher than that near the anode gas output. The maximum temperatures of the cell frame were 623.6 °C for the co-flow type cell and 623.86° for the counter-flow type cell. The maximum temperature of the cell frame was slightly lower than that of the reaction surface.

The polarization percentages of the Nernst loss, the ohmic loss, the cathode polarization loss, and the anode polarization loss are listed in Table 4. The cathode polarization is the largest polarization component. The Nernst loss is the second largest polarization component. The Nernst loss shows the largest polarization difference between co-flow and counter-flow.

Gas distribution in the 100 cm^2 single cell

The velocity distributions of anode gas at 150 mA/cm^2 are shown in Fig. 10. Fig. 10(a) presents perspective and side views of the anode gas flow channel. Fig. 10(b) shows the distribution of the velocity magnitude at the center of the gas flow channel (Section B). Fig. 10(c) shows the velocity distribution of Section D. Due to the low Reynold's number, gas flow in the flow channels is in laminar form (Re = 0.68), as a result, a velocity profile is parabolic in shape. Fig. 10(d) shows the velocity distribution at the gas input channel (Section C). After gas was distributed at the gas distribution space, the gas flow though the gas flow channel formed by the metallic cell frames. At the anode side, the velocity of the anode gas increases along the gas flow direction, because H$_2$O and CO$_2$ were generated from the electrochemical reaction of the anode side.

The mole fractions of the anode and cathode gases with co-flow and counter-flow at 150 mA/cm^2 and 620 °C are presented in Fig. 11. The mole fractions of H$_2$ in the anode flow channel decreased with the electrochemical reaction. The mole fractions of CO$_2$, H$_2$O decreased along the flow channel. The mole fractions of CO decreased slightly along the flow channel. Along the anode gas flow direction, the mole fractions of CO$_2$ and O$_2$ decreased monotonically.

The mole fractions of the anode and cathode gases on the reaction surface are shown in Fig. 12. Because of the effect of the gas diffusivity, the shape of the distribution of the co-flow type cell was different from the shape of the counter-flow type cell. The diffusivity of the anode gases was greater than that of the cathode gases. Therefore, the wavy shape of the CO$_2$ mole fraction in Fig. 12(a) is more pronounced than that of the H$_2$ mole fraction in Fig. 12(b).

The distributions of the total resistance including the anode reaction resistance, cathode reaction resistance and the ohmic resistance of the co-flow type and counter-flow
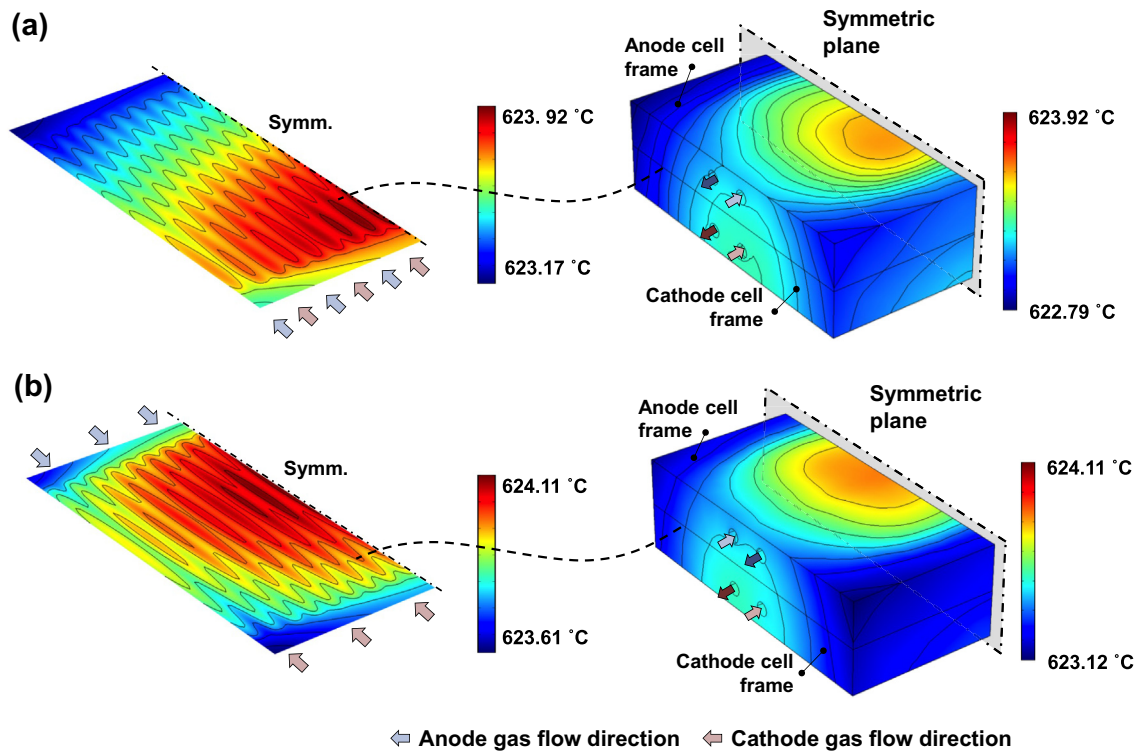
Fig. 9 – Temperature distribution of the reaction layer and cell frames at 150 mA/cm² and 620 °C: (a) co-flow and and (b) counter-flow.

Table 4 – Voltage and polarization percentages of the single cell at 150 mA/cm²

Flow type	Voltage (V)	Polarization percentage (%)			
		Nernst loss	Ohmic loss	Cathode polarization	Anode polarization
Co-flow	0.817	32.4%	20.9%	38.8%	9.2%
Counter-flow	0.823	31.0%	20.6%	37.9%	8.9%
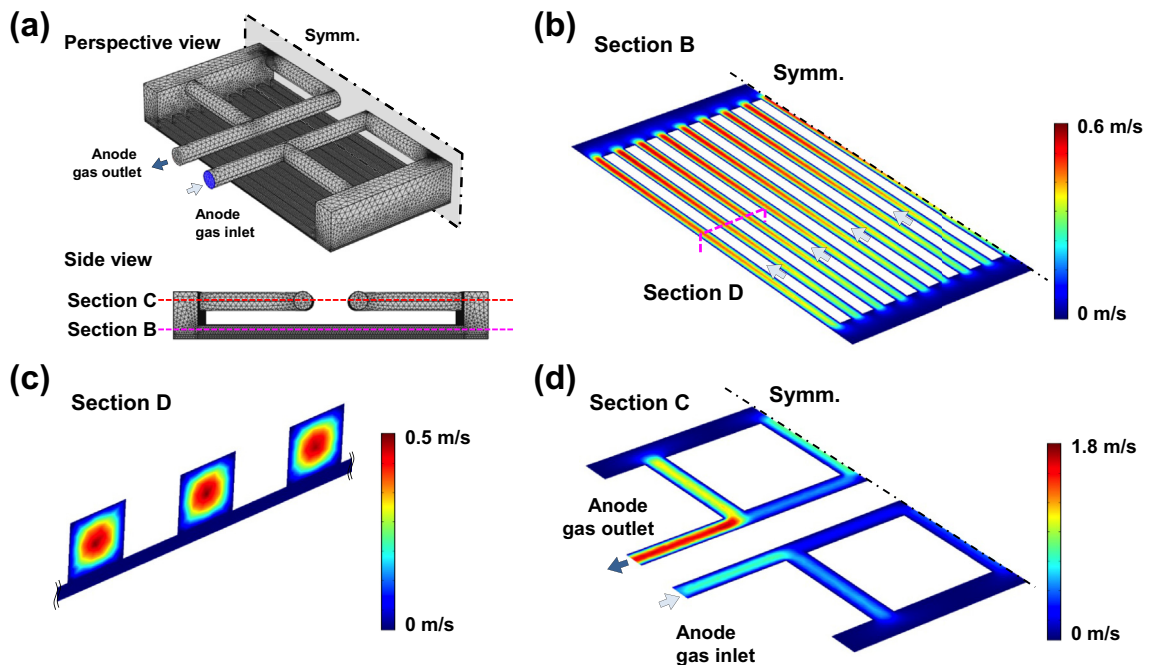
Fig. 10 – Distribution of anode gas velocity at 150 mA/cm²: (a) Anode gas flow channel (b) Velocity magnitude distribution at the center of the gas flow channel (c) Velocity distribution of section D, and (d) Velocity distribution at the gas input channel.
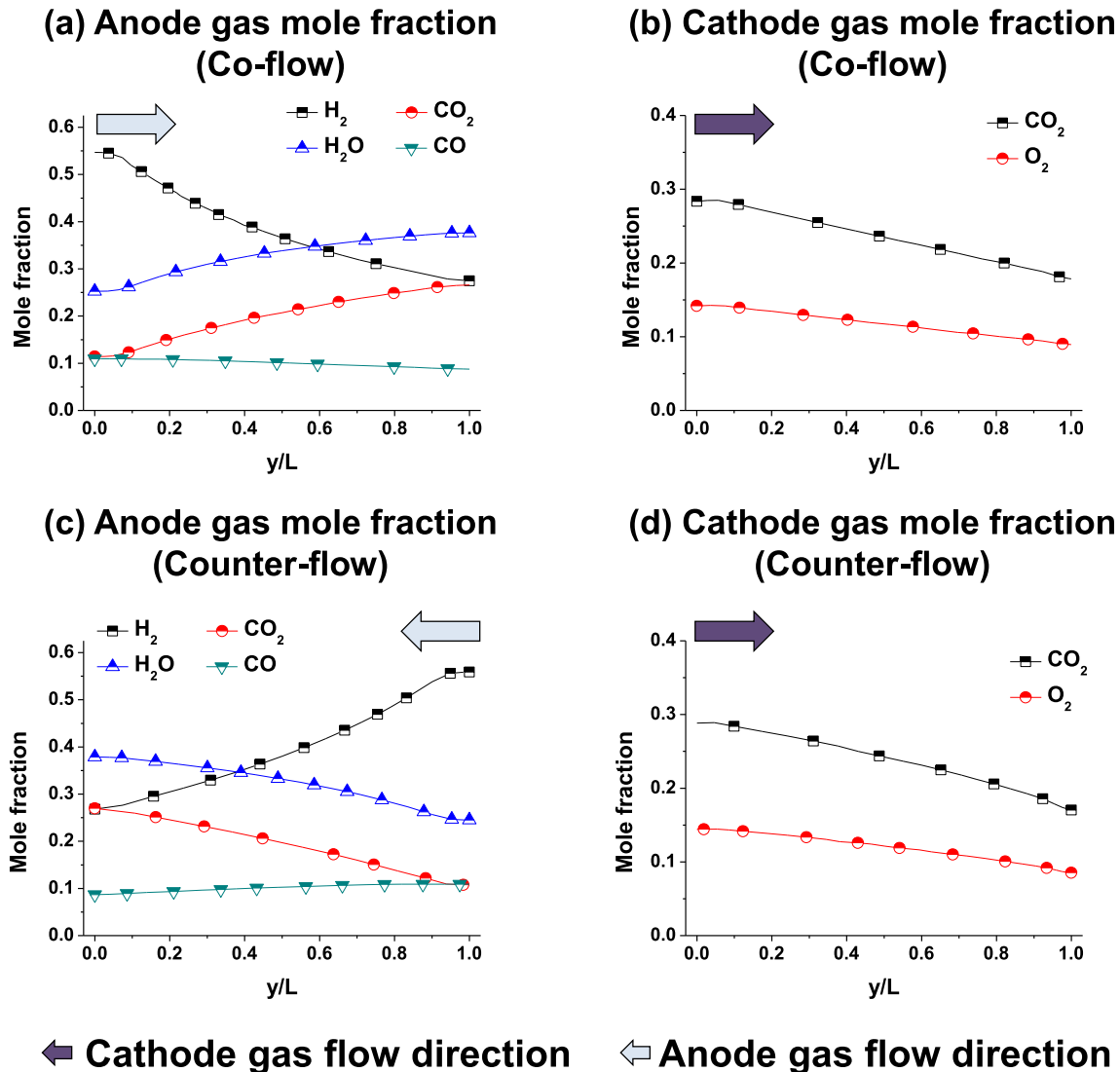
Fig. 11 – Gas mole fractions along the gas flow direction at 150 mA/cm²: (a) cathode reaction resistance (co-flow) (b) anode reaction resistance (co-flow) (c) cathode reaction resistance (Counter-flow), and (d) anode reaction resistance (counter-flow).

type cells are presented in Fig. 13 (a) and (b), respectively. The total resistance shows similar distributions. In the counter-flow type cell, the anode reaction resistance increases along the cathode gas flow direction, and the cathode reaction resistance increases along the cathode gas flow direction. The total resistance of the counter-flow type cell at the cathode gas exit is slightly larger than that of the co-flow type cell.

However, the current density distribution shows different characteristics. The local current density was calculated using Eq. (11). The distribution of E_{eq} determined using Eq. (7) is plotted in Fig. 14. E_{eq} is high near the anode gas input both in co-flow and counter-flow. Due to the distribution of E_{eq}, the distribution of the current density is completely different. A more uniformly distributed current density can be obtained by employing the cell frame with counter-flow.

In the previous studies [11,24,25], the counter-flow type MCFC was not appropriate because of thermal issue: a hotspot occurred near the cathode input site. At the hot spot, the gas cross-over, which is a critical problem of MCFCs can occur.

However, the hot spot did not occur in the cell frame with internal flow channels. The maximum temperature difference in the cell frame was less than 1.1 °C.

Discussion

Improved thermal management using the cell frame with internal flow channels

In this work, cell frames with internal flow channels were employed for improved thermal management of a single cell. In order to investigate the effect of the cell frame with internal flow channels, the simulation model of the conventional cell frame was conducted. In the simulation model of the conventional cell frame, the convection of internal flow channels was not considered. The other simulation conditions were equivalent to the simulation model with internal flow channels.
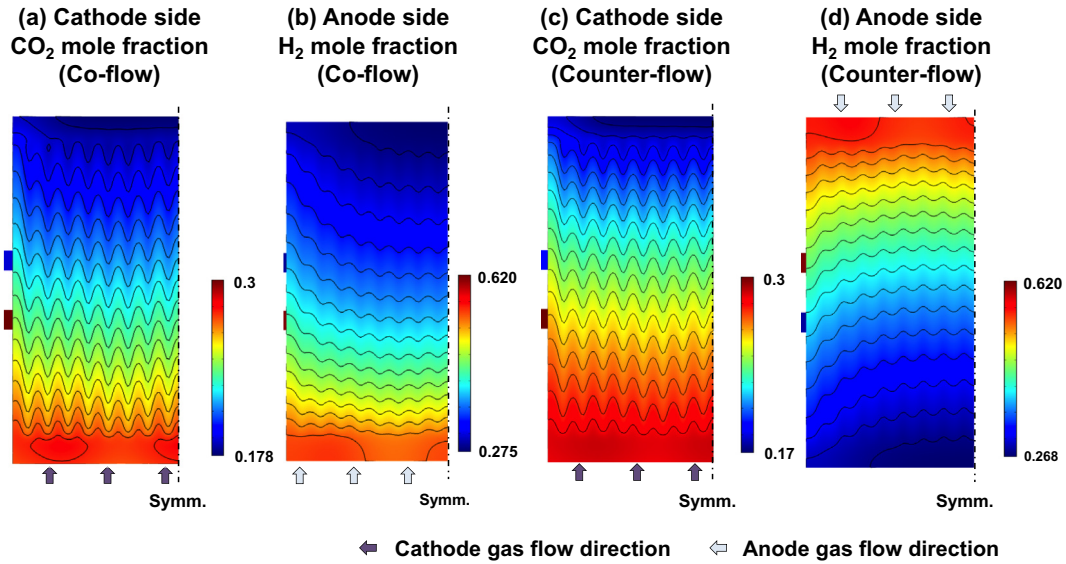
Fig. 12 – Mole fraction of anode and cathode gases on the reaction surface at 150 mA/cm^2: (a) cathode side CO$_2$ mole fraction (co-flow) (b) anode side H$_2$ mole fraction (co-flow) (c) cathode side CO$_2$ mole fraction (counter-flow), and (d) anode side H$_2$ mole fraction (counter-flow).

Fig. 15 compares the maximum temperature in the cell frame with internal flow channels with that in the conventional cell frame. The maximum temperature increases sharply in the high current density regions because the heat from the reaction is proportional to the square of the current density. As demonstrated in Fig. 15(a) and (b), the temperature of the cell frame with internal flow channels is less than that of the conventional cell frame. In particular, the temperature difference between the conventional cell frame and the cell frame with internal flow channels increases as the current density increases. The temperature distribution of the cell frame also decreased using the cell frame with internal flow channels. These results indicate that the cell frame with internal flow channels offers advantages in terms of thermal management.

Current density distribution along the normal direction to the flow direction

The current density distributions along the normal direction of the gas flow direction at the center of the reaction surface (D$_1$-D$_2$, D$_3$-D$_4$) are presented in Fig. 16(a) and (b). The wavy shape of the current density distribution is caused by the gas flow channel. Around the gas flow channel, reactive gases are diffused to electrodes. Because the diffusion coefficient of the cathode gas (D$_{CO_2}$ = 1.183 × 10^{-4} m^2/s) is larger than that of the anode gas (D$_{H_2}$ = 4.615 × 10^{-4} m^2/s), the wavy shapes of the mole fraction in the cathode side shown in Fig. 12 are heavier than those in the anode side. These wavy shapes of the gas mole fractions results in the wavy shape of the total
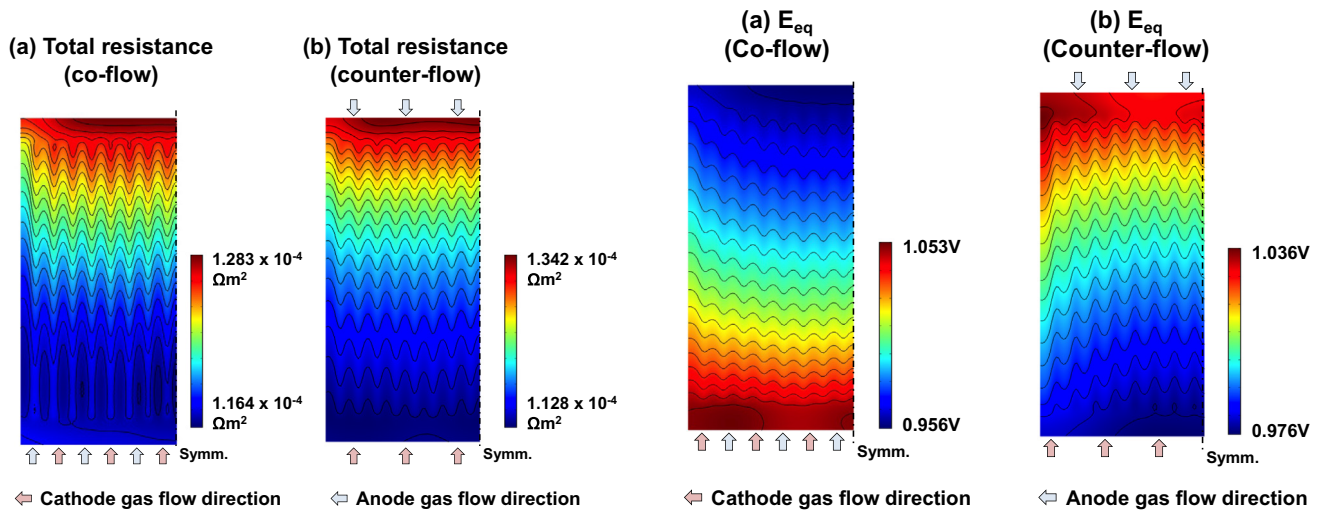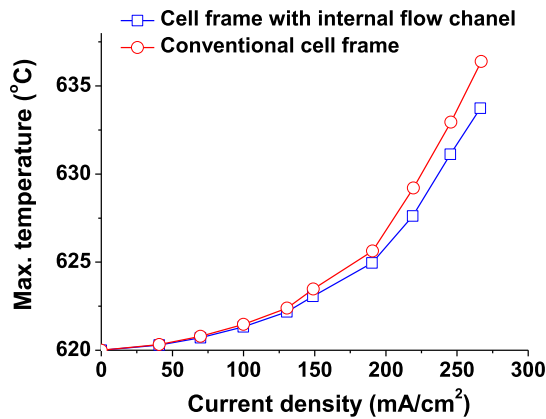

Fig. 13 – Total polarization resistance at 150 mA/cm^2: (a) Co-flow type and (b) Counter-flow type.

Fig. 14 – Equilibrium cell potentials at 150 mA/cm^2: (a) Co-flow type and (b) Counter-flow type.
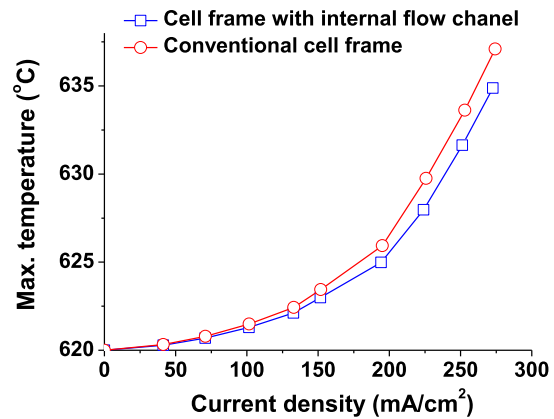
(a) Co-flow

(b) Counter-flow

Fig. 15 – Comparison of the maximum temperature in the cell frame with internal flow channels and in the conventional cell frame: (a) co-flow and (b) counter-flow.

polarization resistance shown in Fig. 13. Finally, the local current density was distributed with wavy shape.

Near the side of the reaction surface (D_2, D_4), the current density increases slightly. At the center (D_1, D_3), the reaction gas can diffuse in all directions. The gases at the side of the cell frame cannot diffuse in the transverse direction. The H_2 mole fraction of the side of the cell frame is higher than in other locations. The reaction resistance is small near D_2 and D_4. Finally, the current density near D_2 and D_4 is higher than near D_1 and D_3.

### Effects of the gas utilization on the distribution of the current density

IV characteristics of the single cell are affected by the gas utilization. In addition, the current density distribution varies with respect to the gas utilization. To investigate the effect of the gas utilization on the current density distribution, the simulation was conducted with other values of gas utilization. The operating temperature was 620 °C and the other operating conditions were the same as those used in the previous simulation.
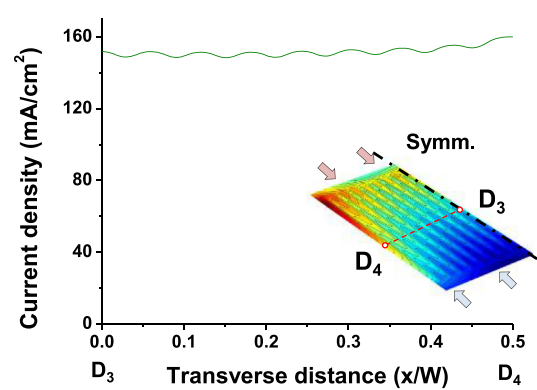
The current density distributions at 150 mA/cm^2 are presented in Fig. 17(a) and (b). In the cell frame cell with co-flow, the current density reached its highest value in the anode gas inlet. Along the gas flow direction, the polarization increases. The current density decreased monotonically from the gas inlet to the gas outlet. For high gas utilization, the difference between the current density at the gas inlet and outlet increased because the polarization components increased along the gas flow direction. In the cell frame cell with co-flow, increasing the flow rate of the input gas (i.e., decreasing the gas utilization) increased the uniformity of the current density distribution.

Fig. 17(b) shows the current density distribution at 150 mA/cm^2 for the counter-flow type cell, which exhibits a different

(a) Co-flow
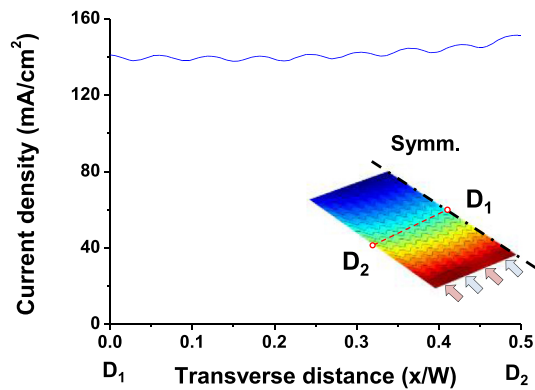
(b) Counter-flow

⇦ **Anode gas flow direction**   ⇦ **Cathode gas flow direction**

Fig. 16 – Current density distribution along the normal direction of the gas flow direction at 150 mA/cm²: (a) co-flow type and (b) counter-flow type cells.
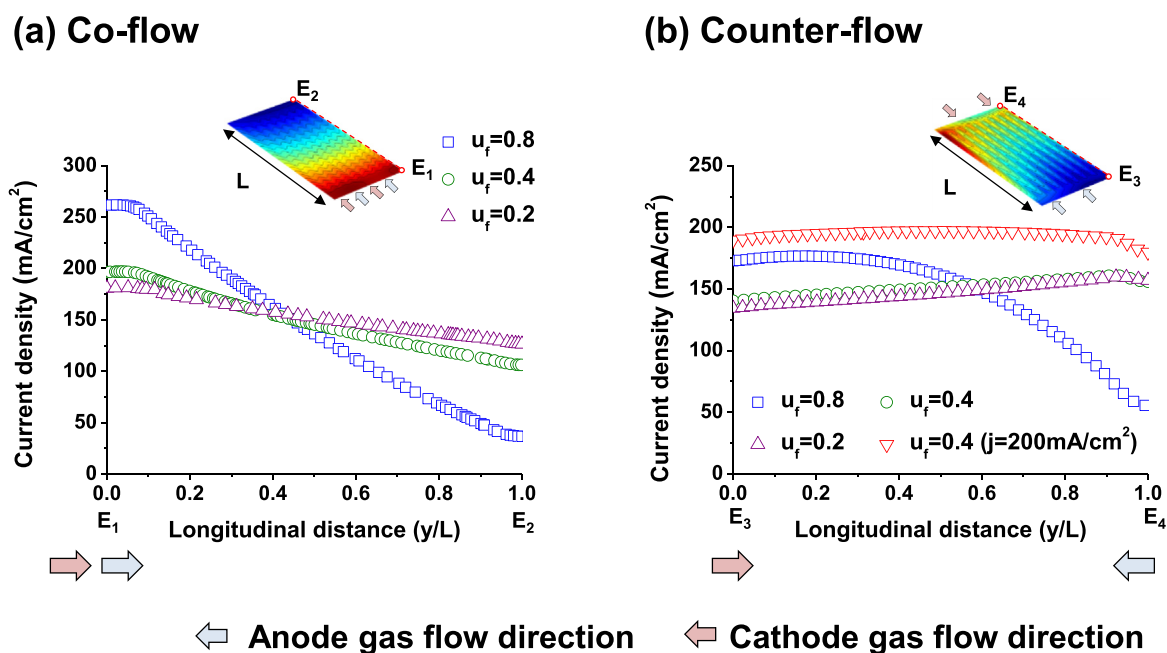
Fig. 17 – Distribution of the current density along the gas flow direction at 150 mA/cm^2: (a) co-flow type and (b) counter-flow type cell.

tendency. At low gas utilization, the current density decreased along the anode gas flow direction. In contrast, at high gas utilization, the current density increased along the anode gas flow direction. The current density distribution is affected by the cathode polarization, because the cathode polarization is the largest polarization component. At the high gas utilization, the cathode polarization increased along the cathode gas flow direction. Therefore the current density decreased along the cathode gas flow direction at high gas utilization.

By controlling the average current density or the gas utilization, a more uniformly distributed current density can be obtained. The current density distribution of 200 mA/cm^2 with the other conditions being the same as those in Table 1 is shown in Fig. 17(b). The current density is more uniformly distributed than for the other cases. A more uniformly distributed current density will result in more uniform electrolyte consumption and more enhanced long-term operation capability. In order to investigate the effect of the current density distribution in the single cell, analysis of the existing amount of the electrolyte in the anode, cathode, and matrix using inductively coupled plasma (ICP) spectroscopy and atomic absorption spectroscopy (AAS) is required [26].

Conclusion

In this work, three-dimensional CFD analysis was conducted to investigate the effect of the flow direction on a 100 cm^2 single cell with internal flow channels for MCFCs. The flow channels were modeled three-dimensionally without employing porous media approach. The temperature, current density and mole fraction distributions of each gas were investigated using the computational fluid dynamics.

The co-flow type and counter-flow type cells can be operated without any hot-spots. The cell frame with internal flow channels showed improved thermal characteristics. The performance difference between the counter-flow type and the co-flow type cell was 4 mV for the experimental results and 6 mV for the simulation result. However, the current density exhibited different tendencies. For the co-flow type cell, the current density decreased monotonically along the flow direction, whereas for the counter-flow type cell, the current density exhibited a more uniform distribution. By controlling the operation conditions such as the average current density or the gas utilization, a uniform current density can be obtained in the counter-flow type cell, which will result in enhanced long-term operation capability.

REFERENCES

[1] O'Hyare R, Cha SW, Collela W, Prinz FB. Fuel cells — fundamentals. New York: John Wiley & Sons; 2006.
[2] Wolf TL, Wilemski G. Molten carbonate fuel cell performance model. J Electrochem Soc 1983;130(1):48–55.

[3] Yuh C, Selman J. The polarization of molten carbonate fuel cell electrodes I. Analysis of steady-state polarization data. J Electrochem Soc 1991;138(12):3642–8.

[4] Bosio B, Costamagna P, Parodi F. Modeling and experimentation of molten carbonate fuel cell reactors in a scale-up process. Chem Eng Sci 1999;54(13–14):2907–16.

[5] Morita H, Komoda M, Mugikura Y, Izaki Y, Watanabe T, Masuda Y, et al. Performance analysis of molten carbonate fuel cell using a Li/Na electrolyte. J Power Sources 2002;112(2):509–18.

[6] He W, Chen Q. Three-dimensional simulation of a molten carbonate fuel cell stack under transient conditions. J Power Sources 1998;73(2):182–92.

[7] Koh J-H, Seo H-K, Yoo Y-S, Lim HC. Consideration of numerical simulation parameters and heat transfer models for a molten carbonate fuel cell stack. Chem Eng J 2002;87(3):367–79.

[8] Hirata H, Nakagaki T, Hori M. Effect of gas channel height on gas flow and gas diffusion in a molten carbonate fuel cell stack. J Power Sources 1999;83(1–2):41–9.

[9] Kim M-H, Park H-K, Chung G-Y, Lim H-C, Nam S-W, Lim T-H, et al. Effects of water-gas shift reaction on simulated performance of a molten carbonate fuel cell. J Power Sources 2002;103(2):245–52.

[10] Ma Z, Jeter SM, Abdel-Khalik SI. Modeling the transport processes within multichannel molten carbonate fuel cells. Int J Hydrogen Energy 2003;28(1):85–97.

[11] Kim YJ, Chang IG, Lee TW, Chung MK. Effects of relative gas flow direction in the anode and cathode on the performance characteristics of a Molten Carbonate Fuel Cell. Fuel 2010;89(5):1019–28.

[12] Kim H, Bae J, Choi D. An analysis for a molten carbonate fuel cell of complex geometry using three-dimensional transport equations with electrochemical reactions. Int J Hydrogen Energy 2013;38(11):4782–91.

[13] Yuh C, Colpetzer J, Dickson K, Farooque M, Xu G. Carbonate fuel cell materials. J Mater Eng Perform 2006;15(4):457–62.

[14] Lee S-Y, Kim D-H, Lim H-C, Chung G-Y. Mathematical modeling of a molten carbonate fuel cell (MCFC) stack. Int J Hydrogen Energy 2010;35(23):13096–103.

[15] Brouwer J, Jabbari F, Leal EM, Orr T. Analysis of a molten carbonate fuel cell: numerical modeling and experimental validation. J Power Sources 2006;158(1):213–24.

[16] Song SA, Kim HK, Ham HC, Han J, Nam SW, Yoon SP. Effects of marine atmosphere on the cell performance in molten carbonate fuel cells. J Power Sources 2013;232(0):17–22.

[17] Liu S-F, Chu H-S, Yuan P. Effect of inlet flow maldistribution on the thermal and electrical performance of a molten carbonate fuel cell unit. J Power Sources 2006;161(2):1030–40.

[18] Baranak M, Atakül H. A basic model for analysis of molten carbonate fuel cell behavior. J Power Sources 2007;172(2):831–9.

[19] Koh J-H, Kang BS, Lim HC. Effect of various stack parameters on temperature rise in molten carbonate fuel cell stack operation. J Power Sources 2000;91(2):161–71.

[20] Yoshiba F, Abe T, Watanabe T. Numerical analysis of molten carbonate fuel cell stack performance: diagnosis of internal conditions using cell voltage profiles. J Power Sources 2000;87(1–2):21–7.

[21] Bergman TL, Lavine AS, Incropera FP, DeWitt DP. Fundamentals of heat and mass transfer. 2011.

[22] Kim HS. Three-dimensional fluid flow analysis for flow uniformity of molten carbonate fuel cell stack. Daejeon: KAIST; 2014.

[23] COMSOL Inc.. Comsol multiphysic user's guide. Version. 2012.

[24] Yoshiba F, Ono N, Izaki Y, Watanabe T, Abe T. Numerical analyses of the internal conditions of a molten carbonate fuel cell stack: comparison of stack performances for various gas flow types. J Power Sources 1998;71(1–2):328–36.

[25] He W, Chen Q. Three-dimensional simulation of a molten carbonate fuel cell stack using computational fluid dynamics technique. J Power Sources 1995;55(1):25–32.

[26] Patil KY, Yoon SP, Han J, Lim T-H, Nam SW, Oh I-H. The effect of lithium addition on aluminum-reinforced α-LiAlO2 matrices for molten carbonate fuel cells. Int J Hydrogen Energy 2011;36(10):6237–47.